

# EULER-ADAS: Energy-Efficient & SIMD-Unified Logarithmic-Posit Engine for Precision-Reconfigurable Approximate ADAS Acceleration

Mukul Lokhande <sup>✉</sup>, *Member, IEEE*, Ratko Pilipović <sup>✉</sup>, Omkar Kokane <sup>✉</sup>,  
Adam Teman <sup>✉</sup>, *Senior Member, IEEE*, and Santosh Kumar Vishvakarma <sup>✉</sup>, *Senior Member, IEEE*

**Abstract**—Advanced driver-assistance systems (ADAS) require neural compute engines that deliver low-latency inference under strict power and area constraints. Posit arithmetic is attractive for such accelerators because it provides high numerical fidelity at low precision, but its variable-length regime encoding increases encode/decode cost and exposes the datapath to large regime-field fault effects. This paper presents EULER-ADAS, a SIMD-enabled logarithmic bounded-Posit neural compute engine for energy-efficient and reliability-aware ADAS acceleration. The proposed datapath combines bounded-regime Posit representation, stage-adaptive logarithmic mantissa multiplication with bit truncation, and a SIMD-shared quire accumulation path supporting Posit-(8,0), Posit-(16,1), and Posit-(32,2) execution. The unified architecture enables  $4\times$  Posit-8,  $2\times$  Posit-16, or  $1\times$  Posit-32 operation without duplicating precision-specific hardware. FPGA implementation shows that the proposed configurations reduce LUT count by up to 41.4%, delay by up to 76.1%, and power by up to 71.9% relative to exact Posit neural compute engines, while achieving up to  $10\times$  lower energy-delay product than radix-4 Booth-based Posit multipliers. In 28-nm CMOS, the bounded variants occupy 0.013-0.016 mm<sup>2</sup>, consume 19.8-22.1 mW, and operate at up to 1.84 GHz. Application-level evaluation across image-classification, ADAS, and edge-inference workloads shows that the evaluated Posit-16 and Posit-32 configurations remain within about 1.5 percentage points of FP32 accuracy. A Tiny-YOLOv3 prototype on Pynq-Z2 achieves 78 ms latency at 0.29 W and 22.6 mJ/frame, demonstrating the suitability of EULER-ADAS for low-power real-time ADAS inference.

**Index Terms**—SIMD Posit arithmetic, mixed precision, approximate multiplier, logarithmic multiplier, ADAS, bounded Posit

Manuscript received XXXX; revised XXXX.

This research was supported by the Slovenian Research Agency under Grant P2-0359 (National Research Program on Pervasive computing), and Israeli Ministry Science, Innovation and Technology (MOST) under the Project wAIve. This work was also supported by the Special Manpower Development Program for Chip to Start-Up (SMDP-C2S), Ministry of Electronics and Information Technology (MeitY), Government of India, under Grant EE-9/2/21-R&D-E.

Mukul Lokhande, Omkar Kokane, and Santosh K. Vishvakarma are with the NSDCS Research Group, Dept. of Electrical Engineering, Indian Institute of Technology Indore, Indore, India. Ratko Pilipović is with the Faculty of Computer and Information Science, University of Ljubljana, Ljubljana, Slovenia. Adam Teman is with EnICS Labs, Bar-Ilan Univ., Ramat Gan 5290002, Israel.

This work extends O. Kokane, M. Lokhande, G. Raut, A. Teman and S. K. Vishvakarma, "LPRE: Logarithmic Posit-enabled Reconfigurable edge-AI Engine", IEEE International Symposium on Circuits and Systems (ISCAS), London, United Kingdom, pp. 1-5, 2025. The prior conference publication focused on a reconfigurable logarithmic Posit arithmetic architecture that preserves application-level accuracy relative to FP32 while achieving significant hardware savings. This manuscript extends that work along three axes: combining logarithmic approximation with bit-truncation for accuracy-tunable mantissa arithmetic, adopting B-Posit representation to eliminate the variable-length encoding and decoding overhead, and introducing a SIMD-enabled accumulation datapath. To the best of our knowledge, this represents the first approximate logarithmic multiplier designed for the bounded Posit format. The extended evaluation further covers a comprehensive set of ADAS workloads to validate the proposed engine across representative application scenarios.

Corr. author: Ratko Pilipović (e-mail: ratko.pilipovic@fri.uni-lj.si).

## I. INTRODUCTION

The deployment of autonomous vehicles and advanced driver-assistance systems (ADAS) relies on perception pipelines that must interpret complex driving environments under strict latency and power constraints. These pipelines increasingly depend on deep neural networks for tasks ranging from object detection [1] to autonomous navigation [2], motivating domain-specific accelerators (DSAs) that combine a host processor, on-chip memory hierarchy, and a dedicated neural compute engine (NCE), as illustrated in Fig. 1. Within such accelerators, data movement and arithmetic dominate energy consumption: memory accesses can account for more than 80% of system energy [3], while multiply-accumulate (MAC) units occupy a large fraction of the arithmetic core area and active power [4]. Consequently, the numerical format used by the NCE becomes a central design lever, as it directly affects memory bandwidth, arithmetic complexity, and inference accuracy.

Low-precision quantization reduces memory traffic and MAC complexity by replacing IEEE 754 floating-point arithmetic with compact fixed-point formats, but this efficiency is often obtained at the cost of reduced numerical fidelity [5], [6]. Posit arithmetic offers a more favorable accuracy-dynamic-range trade-off at low bit widths through variable-length regime field encoding (VLRE), enabling compact representations with dynamic range comparable to wider floating-point formats [7]. In DNN inference, Posit-8 and Posit-16 have been shown to match the accuracy of BFloat16 and FP32, respectively, while reducing memory footprint and improving arithmetic density [8]. However, the same variable-length encoding that gives Posit its dynamic range also complicates hardware decoding and introduces reliability concerns, motivating a closer examination of Posit datapaths for ADAS accelerators.

For ADAS accelerators, numerical efficiency alone is insufficient: the arithmetic datapath must also remain robust under faults [9]. In standard Posit arithmetic, VLRE couples the numerical scale to a variable-length regime field, making the representation sensitive to bit flips in the regime bits. A single regime-field fault can therefore produce a disproportionately large numerical deviation, which is particularly undesirable in safety-relevant perception workloads. Fixed-regime Posit variants reduce this sensitivity [10], but they do so by sacrificing much of the dynamic-range advantage that motivates Posit arithmetic in the first place.

Bounded Posit (B-Posit) [11] provides a more balanced alternative by limiting the maximum regime length rather than removing regime variability entirely. This bounded-regime

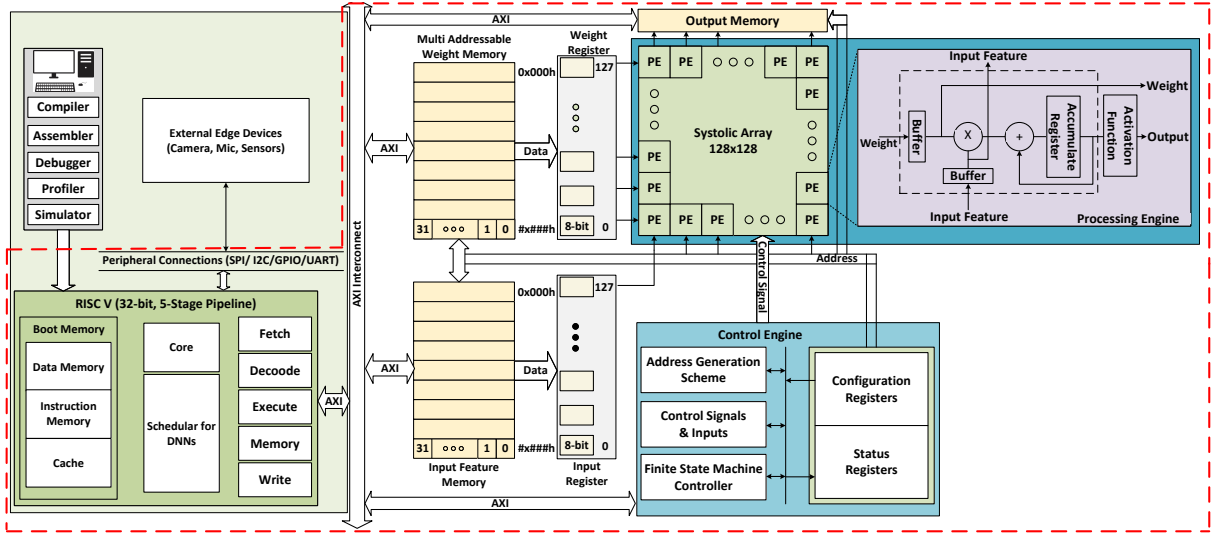


Fig. 1. Domain-specific accelerator SoC architecture.

representation reduces the severity of catastrophic regime-field errors and has been shown to improve soft-error resilience by up to 47.2% relative to standard Posit [12]. At the same time, bounding the regime simplifies operand decoding and result encoding, reducing the hardware overhead of Posit arithmetic. B-Posit therefore addresses two central obstacles to deploying Posit NCEs in ADAS accelerators: reliability under faults and the cost of variable-length encode/decode logic.

While B-Posit reduces the cost and fault sensitivity of Posit encode/decode logic, the arithmetic core of the NCE remains dominated by mantissa multiplication and accumulation. Exact radix-4 Booth multipliers provide high numerical fidelity but impose substantial area, delay, and power overhead, especially in multi-precision SIMD datapaths. Approximate computing offers an attractive alternative because neural inference workloads can tolerate bounded arithmetic error [13]. Among approximate multiplier families, logarithmic multipliers are particularly well suited to compact NCE design because they replace multiplication with addition in the logarithmic domain [14]. However, applying logarithmic multiplication only to the mantissa path leaves other Posit overheads intact, and existing SIMD designs often optimize multiplication without jointly addressing encode/decode and accumulation costs.

This paper presents EULER-ADAS, a SIMD-enabled logarithmic bounded-Posit NCE for energy-efficient and reliability-aware ADAS acceleration. EULER-ADAS jointly optimizes operand decoding, mantissa multiplication, quire accumulation, and result encoding within a unified precision-reconfigurable datapath. The architecture uses bounded Posit representation to reduce variable-length encode/decode overhead and mitigate regime-field fault sensitivity, a stage-adaptive logarithmic multiplier with bit truncation to provide accuracy-cost tuning in the mantissa path, and a SIMD-shared accumulation datapath that supports Posit-(8,0), Posit-(16,1), and Posit-(32,2) execution without duplicating precision-specific hardware.

The main contributions of this paper are as follows:

- We propose EULER-ADAS, the first approximate B-Posit neural compute engine that integrates bounded-regime Posit encode/decode, stage-adaptive logarithmic mantissa multiplication, and SIMD-shared quire accumulation into a unified datapath.
- We introduce a configurable logarithmic Posit multiplication framework in which the multiplier stage count and truncation width act as accuracy-cost knobs across Posit-8, Posit-16, and Posit-32 operating modes.
- We provide FPGA and 28-nm ASIC evaluations showing that the proposed co-designed datapath reduces area, delay, power, and EDP relative to exact Posit and prior approximate NCE baselines.
- We validate the architecture across image classification, ADAS, and edge-inference workloads, including a Tiny-YOLOv3 Pynq-Z2 prototype, showing that the hardware savings are achieved with limited application-level accuracy loss.

The remainder of this paper is organized as follows. Section II reviews related work. Section III presents the theoretical analysis and architectural design of EULER-ADAS. Section IV details the evaluation methodology and results. Section V concludes the paper and outlines directions for future work.

## II. BACKGROUND AND MOTIVATION

### A. Related Work

MAC operations dominate the arithmetic workload of DNN inference, and the multiplier is typically the most expensive component of the MAC datapath in energy, delay, and area [15], [16]. Exact Booth multipliers and full-precision accumulation paths provide high numerical fidelity, but they often exceed the precision required by neural inference workloads [17], [18]. Since DNNs can tolerate bounded arithmetic perturbations, approximate multiplication has emerged as an effective approach for reducing hardware cost while preserving application-level accuracy [19].

Approximate multipliers can be broadly grouped into non-logarithmic and logarithmic designs. Non-logarithmic approaches reduce the complexity of conventional multiplication by simplifying Booth encoding [20]–[22], using approximate compressors in the partial-product reduction tree [23], decomposing operands into smaller segmented multipliers [18], or representing values with stochastic bitstreams [24]. These techniques can reduce area and power, but their benefits are often limited by the remaining partial-product generation and reduction logic. Booth simplification is usually constrained to modest radix choices, compressor-based designs require careful error compensation or bit-position selection, segmented multipliers mainly approximate lower-significance product bits, and stochastic designs suffer from latency and scalability limitations as operand width increases.

Logarithmic approximate multipliers address some of these limitations by following Mitchell’s product approximation [25], which transforms multiplication into addition in the logarithmic domain using a binary logarithm approximation. This structure avoids explicit partial-product generation and can provide larger area and energy savings than many non-logarithmic approximations [26]–[29]. The main drawback is higher arithmetic error, which has motivated correction and refinement techniques [30]. However, prior studies show that DNN inference can often tolerate the uncorrected error of logarithmic multipliers while maintaining accuracy comparable to exact or non-logarithmic approximate designs [28], [31].

The compactness of logarithmic multipliers has led to their use in floating-point [14], [32] and Posit arithmetic [33], where they primarily target mantissa multiplication. In Posit NCEs, however, multiplier-level savings can be limited by the surrounding datapath, including variable-length operand decoding, exponent and regime processing, result encoding, and accumulation. Resource-shared SIMD engines [34], [35] improve multi-precision utilization, but they do not jointly address Posit reliability, bounded-regime encode/decode complexity, approximate mantissa multiplication, and mode-shared accumulation. EULER-ADAS targets this combined design problem by co-designing a stage-adaptive logarithmic mantissa multiplier with a bounded-Posit datapath and a SIMD-shared quire accumulator.

### B. Design Framework for Reliability and Approximation

This subsection establishes the analytical framework used to select the bounded-regime and logarithmic-multiplier parameters of EULER-ADAS. The framework links three design variables: the bounded regime length  $R$ , which controls the severity of regime-field faults; the logarithmic multiplier stage count  $n$ , which controls approximation error; and the truncation width  $m$ , which provides an additional area-accuracy trade-off.

1) *Reliability of Bounded Posit Representation*: A posit value is represented as

$$x = (-1)^s \cdot (\text{used})^k \cdot 2^e \cdot (1 + f), \quad \text{used} = 2^{2^{e_s}}, \quad (1)$$

where  $s$  is the sign bit,  $k$  is the regime value,  $e$  is the exponent, and  $f$  is the fraction. Since the regime term dominates

the dynamic range of posit numbers, any corruption in the regime field can produce a catastrophic change in numerical magnitude. Therefore, bounding the regime directly reduces the sensitivity of the representation to bit-flips. A bounded-regime posit is denoted as

$$\text{bPosit}(N, e_s, R), \quad (2)$$

where  $N$  is the word length,  $e_s$  is the exponent size, and  $R$  is the maximum regime-field width in bits.

Following the soft-error resilience analysis for Posit arithmetic in [12], we characterize the fault sensitivity of bounded Posit using the Expected Catastrophic Error (ECE). ECE measures the expected distortion in logarithmic magnitude between the original value  $x_o$  and the faulty value  $x_f$ :

$$\eta_B = \mathbb{E}[|\log_2 |x_o| - \log_2 |x_f||], \quad (3)$$

The metric can be decomposed into regime and exponent contributions as

$$\eta_B \approx 2^{e_s} \mathbb{E}[|k_o - k_f|] + \mathbb{E}[|e_o - e_f|]. \quad (4)$$

The closed-form ECE for a bounded Posit configuration  $(N, e_s, R)$  is given by:

$$\eta_B(N, e_s, R) = 2^{e_s} [G_1(R) + G_2(R) + G_3(R)] + \frac{2^{e_s} - 1}{2}, \quad (5)$$

where  $G_1(R)$ ,  $G_2(R)$ , and  $G_3(R)$  denote the expected contributions from faults in the regime run bits, the regime terminating bit, and the exponent field, respectively [12]. Since  $\eta_B$  increases monotonically with the regime bound  $R$ , reducing  $R$  lowers the expected catastrophic error:

$$R_1 < R_2 \implies \eta_B(N, e_s, R_1) < \eta_B(N, e_s, R_2). \quad (6)$$

The resilience improvement of bounded Posit relative to standard Posit is expressed through the improvement factor:

$$\Gamma_B(N, e_s, R) = \frac{\eta_{\text{std}}(N, e_s)}{\eta_B(N, e_s, R)}, \quad (7)$$

where  $\Gamma_B > 1$  indicates lower expected catastrophic error than standard Posit. The reliability benefit of bounding the regime comes primarily from limiting the numerical severity of regime-field faults, rather than from reducing the frequency of exceptional values. Thus, B-Posit improves resilience by constraining the magnitude distortion induced by a fault while retaining much of the dynamic-range flexibility of standard Posit. A more detailed analysis of reliability of B-Posit representation is provided in the Supplemental Materials, which accompany paper.

2) *Approximation Error of Logarithmic Multiplication*: For the stage-adaptive logarithmic multiplier, the relative approximation error of an  $n$ -stage implementation is bounded by: [30]

$$RE(n) \leq 2^{-2^n}, \quad (8)$$

with the worst case occurring when both multiplicands have all-one fractional patterns. When operand truncation is also applied, only  $m$  bits after the leading-one position are retained. The combined relative error can then be bounded as

$$RE(n, m) \leq 2^{-2^n} + 2^{-m}, \quad (9)$$

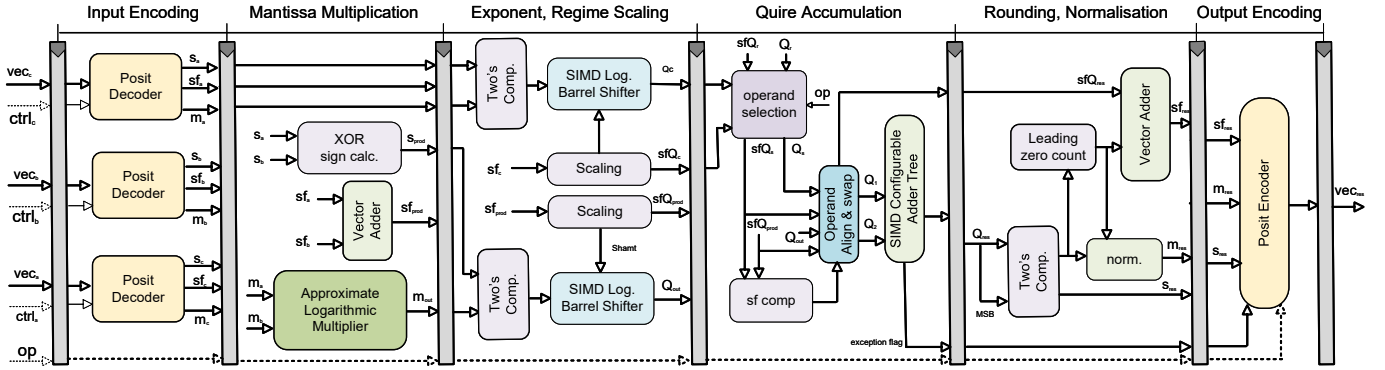


Fig. 2. Detailed datapath of the unified SIMD Logarithmic-Posit neural compute engine (NCE), highlighting the key focus of this work: mantissa multiplication, the SIMD-configurable adder tree, and the decoder/encoder unit.

where the first term captures logarithmic approximation and the second term captures truncation error.

3) *Design-Space Exploration*: Equations (5)-(9) define the three design parameters used in EULER-ADAS: stage count  $n$ , truncation width  $m$ , and bounded regime length  $R$ . The stage count is selected to keep the logarithmic approximation error commensurate with the target precision: for 8-bit Posit,  $n \in \{2, 3\}$  yields  $RE \leq 2^{-4}$  and  $2^{-6}$ , respectively; for 16-bit Posit,  $n \in \{4, 6\}$  provides tighter bounds for the wider mantissa field; and for 32-bit Posit,  $n \in \{8, 12\}$  further reduces approximation error for high-precision execution. The truncation width is selected so that the truncation term  $2^{-m}$  remains controlled relative to the logarithmic approximation term  $2^{-2n}$ , retaining 4 or 5 bits for 8-bit Posit, 8 or 10 bits for 16-bit Posit, and 16 or 20 bits for 32-bit Posit. Finally, the regime bound  $R$  is chosen as the smallest value that preserves the dynamic range required by the target workloads, with  $R = 2$  for Posit-8,  $R = 3$  for Posit-16, and  $R = 5$  for Posit-32. This choice improves fault resilience according to (6) while retaining sufficient dynamic range for inference.

### III. EULER-ADAS: ARCHITECTURE

The EULER-ADAS datapath, shown in Fig. 2, implements a six-stage SIMD pipeline for precision-reconfigurable Posit multiply-accumulate execution. The datapath supports Posit-(8,0), Posit-(16,1), and Posit-(32,2) modes within a shared hardware structure, enabling multi-precision operation without duplicating precision-specific MAC units. Guided by the framework in Section II-B, the architecture combines bounded-Posit encode/decode logic, stage-adaptive logarithmic mantissa multiplication, SIMD exponent and regime scaling, quire-based accumulation, and final rounding and normalization. The six pipeline stages are described below.

**Stage 1: Operand Decoding.** The SIMD input vectors ( $vec\_a, vec\_b, vec\_c$ ) are first decomposed into sign, regime, exponent, and mantissa fields using resource-shared bounded-Posit decoders [11]. The decoding circuitry, shown in Fig. 3(f), exploits the bounded regime length to avoid the long variable-length extraction path of conventional Posit decoders. The regime bits are XORed with the sign bit and mapped into a one-hot representation using simple NOT and AND logic.

This one-hot value selects the exponent scaling through the *EXP\_SIG\_MUX*, while the regime count is recovered through a priority encoder.

Because bounded-Posit operands are stored in two's-complement form, sign-aware extraction is used to recover the constituent fields before arithmetic processing. The raw exponent and regime bits are XORed with the sign bit to generate the final exponent and regime values. As a result, the decoder has a largely bit-width-invariant combinational path, in contrast to standard Posit decoders whose critical paths include chained leading-bit detection, shifting, multiplexing, and addition [4]. This bounded-regime decoding strategy reduces the latency and hardware cost of the operand-processing stage, at the expense of a narrower dynamic range.

**Stage 2: Mantissa Multiplication.** The decoded mantissa fields are processed by SIMD-configurable stage-adaptive logarithmic multipliers (ILMs) [30], as shown in Fig. 4. These multipliers replace the radix-4 Booth mantissa multipliers used in exact Posit datapaths [4]. Instead of generating and reducing partial products, the ILM approximates multiplication through logarithmic-domain addition, substantially reducing multiplier complexity. To further reduce area and power, operand truncation is applied after leading-one detection, retaining only the  $m$  most significant bits required by the selected accuracy mode.

The SIMD multiplier organization follows the high-precision split strategy in Fig. 3(a), allowing the same datapath to support Posit-8, Posit-16, and Posit-32 execution without the operand-bandwidth limitations of low-precision combination schemes [35]. The stage count  $n$  and retained width  $m$  are selected according to the error bounds in Section II-B: Posit-8 uses 2 or 3 ILM stages with 4 or 5 retained bits, Posit-16 uses 4 or 6 stages with 8 or 10 retained bits, and Posit-32 uses 8 or 12 stages with 16 or 20 retained bits. The resulting Posit-level error metrics are reported in Table I.

**Stage 3: Exponent and Regime Scaling.** The product sign is computed through parallel bitwise XOR logic, while the decoded exponent and regime fields are combined using the two-stage addition structure in [4]. The resulting scale value determines the alignment shift required before quire accumulation. To support all precision modes within the same datapath,

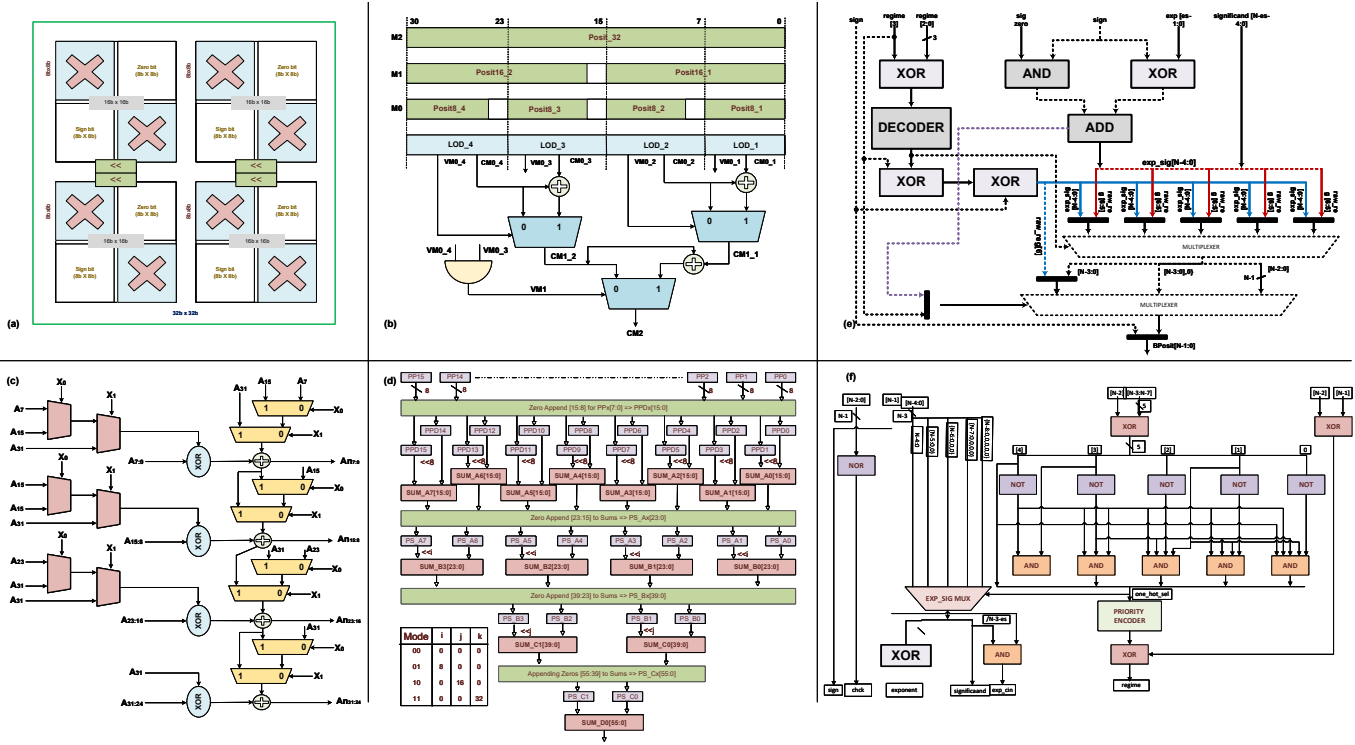


Fig. 3. Detailed internal circuitry of SIMD-configurable compute blocks, illustrating: (a) high-precision split mantissa multiplication, (b) two’s-complement circuitry, (c) leading zero/one detection, (d) restructured SIMD-configurable adder tree, (e) B-Posit encoder, and (f) B-Posit decoder.

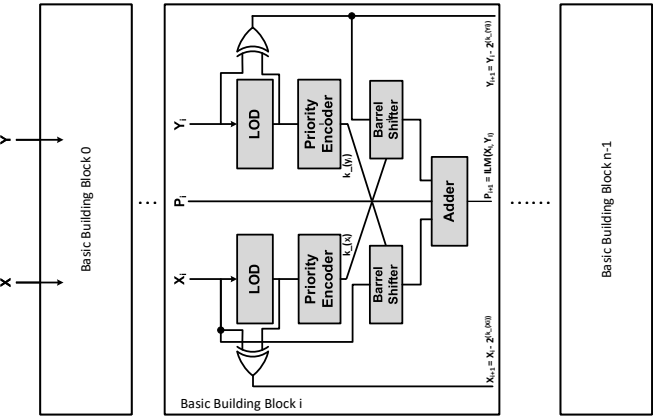


Fig. 4. Pareto-optimal parallel stages for the stage-adaptive logarithmic multiplication approach.

EULER-ADAS uses a SIMD logarithmic barrel shifter [36] that applies the required scaling across Posit-8, Posit-16, and Posit-32 lanes. The computed scaling factors are then forwarded to the accumulation stage.

**Stage 4: Quire Accumulation.** The accumulation stage uses the restructured SIMD-configurable adder tree shown in Fig. 3(d). Partial products from 8-, 16-, and 32-bit modes are accumulated into a shared 128-bit quire, with sign extension and two’s-complement conversion applied according to the product sign and decoded regime information. The exponent and regime scaling factors determine the alignment shift before accumulation, allowing all supported precision modes to reuse

the same reduction topology.

Because mode reconfiguration changes only lane partitioning, operand alignment, and shift distance, the accumulation delay is governed primarily by the adder-tree depth rather than by the number of supported precision modes. This avoids duplicating precision-specific accumulators while preserving sufficient quire width for the worst-case dynamic range across the supported Posit formats. The shared 128-bit quire also delays final rounding until after accumulation, reducing cumulative rounding error.

**Stage 5: Rounding and Normalization.** After quire accumulation, the result is normalized before being packed into the target Posit format. A SIMD-enabled leading-zero-count (LZC) module, shown in Fig. 3(c), determines the normalization shift, while the two’s-complement circuitry in Fig. 3(b) restores the correct signed representation when required. Round-to-nearest-even is then applied using guard, round, and sticky bits to reduce quantization error at the selected output precision.

The control path handles zero, sign inversion, overflow, and special-value propagation, including flush-to-zero, denormals-are-zero, and  $\pm\text{Inf}/\text{NaN}$  cases according to the Posit-2022 handling used in the baseline design. Directed corner-case tests confirm that approximation is confined to mantissa multiplication, while normalization, rounding, and exception handling remain exact.

**Stage 6: Result Encoding.** In the final stage, the bounded-Posit encoder packs the normalized sign, regime, exponent, and mantissa fields into the output Posit word [8]. As shown in Fig. 3(e), the bounded regime length allows the candidate regime, exponent, and fraction fields to be prepared in parallel

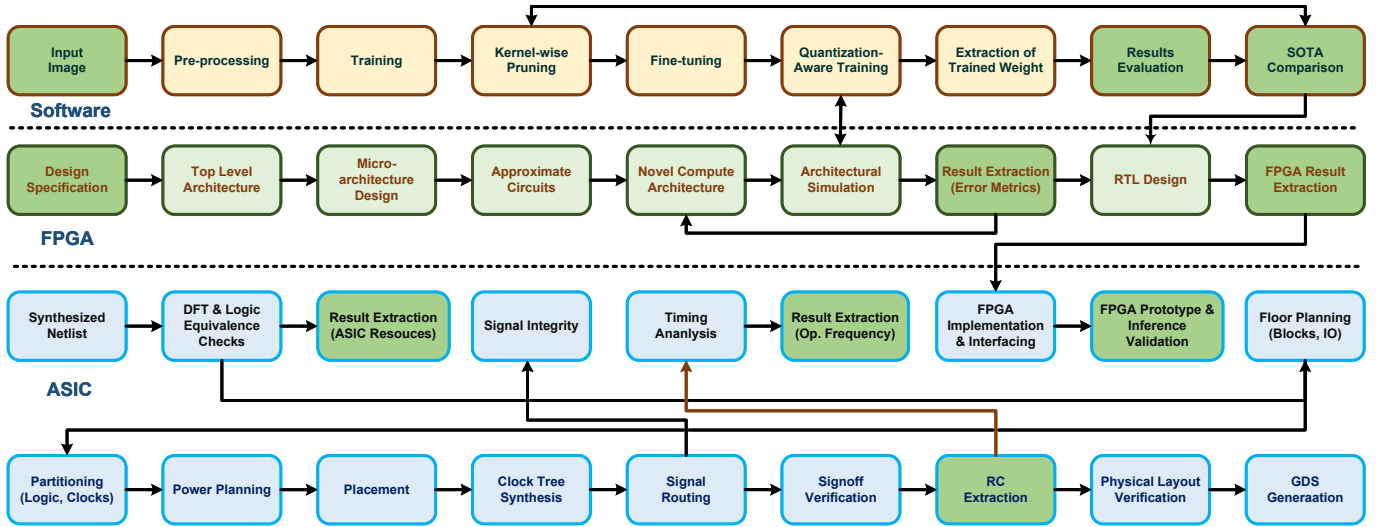


Fig. 5. Detailed methodology/workflow illustrating algorithm-hardware co-design.

and selected through a compact multiplexer structure. The regime width is determined by XORing the lower regime bits with the regime MSB, after which the intermediate regime string is decoded and corrected using the regime sign.

Compared with conventional Posit encoders, which rely on sequential control logic, adders, shifters, and binary decoders, the bounded-Posit encoder has a shorter and more regular critical path. In the implemented datapath, the critical path consists primarily of XOR logic, a binary decoder, and two multiplexer stages, reducing the output-packing overhead that would otherwise limit the benefit of approximate mantissa multiplication.

#### IV. METHODOLOGY & PERFORMANCE EVALUATION

The evaluation methodology, summarized in Fig. 5, combines arithmetic-level modeling, RTL validation, FPGA implementation, ASIC synthesis, and application-level inference experiments. At the arithmetic level, a Python bit-accurate model implements the proposed bounded-Posit and logarithmic-multiplier variants and is used to measure numerical error across scalar and SIMD configurations. The RTL implementation is written in Verilog HDL and verified in QuestaSim against the Python model using matched input vectors. FPGA results are obtained after implementation in AMD Vivado on Xilinx VC707 and PYNQ-Z2 platforms, while ASIC results are obtained using a Cadence RTL-to-GDS flow with Genus synthesis and Innovus place-and-route in a 28-nm CMOS HPC process. Application-level experiments use the same bit-accurate arithmetic model to evaluate the accuracy impact of the proposed configurations on representative ADAS and edge-inference workloads.

##### A. Arithmetic Error Evaluation

To quantify the arithmetic error introduced by the proposed approximations, four metrics are evaluated across all configurations: mean squared error (MSE), mean absolute error (MAE), normalized mean error distance (NMED), and mean

relative error distance (MRED). Each configuration is denoted  $b_{x\_LP-n\_Tm}$ , where  $x$  is the upper bound on regime bits,  $n$  is the logarithmic multiplier stage count, and  $m$  is the number of retained bits after truncation. Error metrics are obtained for logarithmic Posit multipliers in 2- and 3-stage configurations for 8-bit Posit, 4- and 6-stage configurations for 16-bit Posit, and 8- and 12-stage configurations for 32-bit Posit. Each variant is compared against exact radix-4 Booth-based Posit multiplication, and SIMD configurations are additionally evaluated in 8b/16b and 8b/16b/32b operating modes.

Table I shows that increasing the logarithmic multiplier stage count generally improves arithmetic accuracy, while truncation introduces a modest additional error that can be traded for lower hardware cost. The lowest-error entries in each precision group are highlighted in bold. Increasing the retained width  $m$  reduces truncation error, although its effect is smaller than the change caused by the logarithmic approximation stage count. Bounded-regime variants incur additional error because restricting the regime length narrows the representable dynamic range relative to standard Posit. The SIMD variants exhibit larger arithmetic error than their scalar counterparts, which motivates the application-level validation reported later in Section IV-D. Since MSE penalizes large-magnitude deviations and aligns with the  $\ell_2$  structure commonly used in DNN training objectives, it is used as the primary aggregate fidelity criterion, while MAE, NMED, and MRED are also reported for completeness.

##### B. FPGA Evaluation

Table II compares the proposed scalar and SIMD design variants against exact radix-4 Booth-based Posit multipliers and prior SIMD NCE implementations. Bold entries mark the best or text-discussed proposed values within each precision group. Relative to the exact Posit baseline, the best EULER-ADAS configurations achieve up to  $3\times$ ,  $6\times$ , and  $10\times$  lower

TABLE I  
ERROR ANALYSIS OF LOGARITHMIC POSIT MULTIPLIERS COMPARED TO  
ACCURATE RADIX-4 BOOTH-BASED POSIT MULTIPLIERS.

Format	Multiplier	Stage	MSE	MAE	NMED ( $\times 10^3$ )	MRED (%)
Scalar 8-bit	LP-2 (L-1)	2	0.103	0.257	20.4	10.5
	<b>LP-3 (L-2)</b>	<b>3</b>	<b>0.089</b>	<b>0.238</b>	<b>19.6</b>	<b>9.2</b>
	LP-3_T4 (L-21)	3	0.098	0.251	20.5	9.8
	LP-3_T5 (L-22)	3	0.094	0.244	20.0	9.4
	b2_LP-2 (L-1b)	2	0.109	0.266	21.3	11.4
	b2_LP-3 (L-2b)	3	0.096	0.246	20.6	9.9
	b2_LP-3_T4 (L-21b)	3	0.104	0.262	21.4	10.5
b2_LP-3_T5 (L-22b)	3	0.101	0.252	20.8	10.0	
Scalar 16-bit	LP-4 (L-1)	4	0.051	0.181	14.4	6.8
	<b>LP-6 (L-2)</b>	<b>6</b>	<b>0.024</b>	<b>0.124</b>	<b>9.9</b>	<b>4.3</b>
	LP-6_T8 (L-21)	6	0.031	0.142	11.1	5.0
	LP-6_T10 (L-22)	6	0.028	0.134	10.4	4.6
	b3_LP-4 (L-1b)	4	0.057	0.191	15.3	7.3
	b3_LP-6 (L-2b)	6	0.029	0.137	10.7	4.7
	b3_LP-6_T8 (L-21b)	6	0.036	0.150	12.1	5.5
b3_LP-6_T10 (L-22b)	6	0.032	0.143	11.2	5.0	
SIMD (8b/16b)	LP-4 (L-1)	4	0.118	0.275	17.8	8.4
	<b>LP-6 (L-2)</b>	<b>6</b>	<b>0.058</b>	<b>0.193</b>	<b>12.9</b>	<b>5.8</b>
	LP-6_T8 (L-21)	6	0.072	0.217	14.3	6.7
	LP-6_T10 (L-22)	6	0.065	0.206	13.5	6.2
	b3_LP-4 (L-1b)	4	0.127	0.287	18.9	9.1
	b3_LP-6 (L-2b)	6	0.067	0.210	13.9	6.3
	b3_LP-6_T8 (L-21b)	6	0.081	0.226	15.2	7.1
b3_LP-6_T10 (L-22b)	6	0.073	0.215	14.3	6.5	
Scalar 32-bit	LP-8 (L-1)	8	0.064	0.202	12.6	5.7
	<b>LP-12 (L-2)</b>	<b>12</b>	<b>0.026</b>	<b>0.129</b>	<b>8.9</b>	<b>3.9</b>
	LP-12_T16 (L-21)	12	0.034	0.147	9.9	4.4
	LP-12_T20 (L-22)	12	0.031	0.139	9.3	4.1
	b5_LP-8 (L-1b)	8	0.071	0.213	13.4	6.1
	b5_LP-12 (L-2b)	12	0.031	0.142	9.5	4.3
	b5_LP-12_T16 (L-21b)	12	0.039	0.155	10.6	4.8
b5_LP-12_T20 (L-22b)	12	0.035	0.148	9.8	4.4	
SIMD (8b/16b/32b)	LP-8 (L-1)	8	0.148	0.307	18.9	8.8
	<b>LP-12 (L-2)</b>	<b>12</b>	<b>0.123</b>	<b>0.280</b>	<b>17.4</b>	<b>8.1</b>
	LP-12_T16 (L-21)	12	0.134	0.295	18.3	8.5
	LP-12_T20 (L-22)	12	0.128	0.287	17.7	8.2
	b5_LP-8 (L-1b)	8	0.158	0.318	19.7	9.2
	b5_LP-12 (L-2b)	12	0.129	0.288	17.9	8.4
	b5_LP-12_T16 (L-21b)	12	0.138	0.300	18.6	8.7
b5_LP-12_T20 (L-22b)	12	0.133	0.292	18.1	8.4	

energy-delay product (EDP) for the 8-bit, 16-bit, and 32-bit scalar cases, respectively.

The FPGA results isolate the effect of the three design parameters introduced in Section II-B. Increasing the logarithmic multiplier stage count improves arithmetic accuracy but increases LUT utilization, critical-path delay, and power. Operand truncation partially offsets this cost by reducing mantissa datapath width, with only a modest increase in arithmetic error. Bounding the regime field has the largest impact on the surrounding Posit datapath, reducing the cost of operand decoding and result encoding rather than only the multiplier. This confirms that encode/decode simplification is an important source of the overall FPGA savings.

The SIMD variants of EULER-ADAS require fewer LUTs than the TCAS-II'24 [35], TVLSI'22 [37], and TCAS-II'22 [4] designs, while also reducing power relative to these prior

TABLE II  
COMPARATIVE FPGA RESOURCE CONSUMPTION AGAINST  
STATE-OF-THE-ART SIMD NEURAL COMPUTE ENGINES.

Format	Multiplier	LUTs	FFs	Delay (ns)	Power (mW)	EDP (a.Js)
Scalar 8-bit	Accurate (R4BM)	517	175	2.69	93	0.67
	LP-2 (L-1)	414	141	1.9	64.3	0.24
	LP-3 (L-2)	438	149	2.01	70.1	0.29
	LP-3_T4 (L-21)	409	139	1.87	63.2	0.23
	LP-3_T5 (L-22)	416	141	1.89	64.6	0.24
	b2_LP-2 (L-1b)	306	105	1.07	29.58	0.17
	b2_LP-3 (L-2b)	322	110	1.15	33.4	0.24
	<b>b2_LP-3_T4 (L-21b)</b>	<b>303</b>	<b>98</b>	<b>1.04</b>	<b>29.1</b>	<b>0.16</b>
	b2_LP-3_T5 (L-22b)	310	112	1.1	30.4	0.19
	Scalar 16-bit	Accurate (R4BM)	1874	528	4.35	159
LP-4 (L-1)		1495	412	2.77	102	0.79
LP-6 (L-2)		1600	440	2.96	109.9	0.97
LP-6_T8 (L-21)		1478	406	2.73	100.4	0.75
LP-6_T10 (L-22)		1510	417	2.79	103.5	0.81
b3_LP-4 (L-1b)		784	208	1.86	76.4	0.53
b3_LP-6 (L-2b)		824	225	1.93	79.5	0.62
<b>b3_LP-6_T8 (L-21b)</b>		<b>752</b>	<b>217</b>	<b>1.83</b>	<b>73.2</b>	<b>0.48</b>
b3_LP-6_T10 (L-22b)		763	189	1.88	75.3	0.51
SIMD (8b/16b)		Accurate (R4BM)	2486	801	5.1	214
	LP-4 (L-1)	1702	525	3.13	118.9	1.17
	LP-6 (L-2)	1810	558	3.35	127.8	1.45
	LP-6_T8 (L-21)	1680	518	3.09	116.6	1.11
	LP-6_T10 (L-22)	1716	530	3.16	120.5	1.2
	b3_LP-4 (L-1b)	1182	389	1.82	<b>59.6</b>	0.67
	b3_LP-6 (L-2b)	1260	406	1.97	67.2	0.86
	<b>b3_LP-6_T8 (L-21b)</b>	<b>1157</b>	<b>353</b>	<b>1.75</b>	60.8	<b>0.62</b>
	b3_LP-6_T10 (L-22b)	1209	392	1.80	62.9	0.69
	Scalar 32-bit	Accurate (R4BM)	4134	1580	10.6	402
LP-8 (L-1)		3510	1330	4.4	227	4.4
LP-12 (L-2)		3730	1415	4.95	242	5.9
LP-12_T16 (L-21)		3480	1320	4.35	224.5	4.25
LP-12_T20 (L-22)		3520	1335	4.4	227.5	4.45
<b>b5_LP-8 (L-1b)</b>		<b>2420</b>	925	2.53	<b>113</b>	3.62
b5_LP-12 (L-2b)		2598	992	2.92	128	<b>3.45</b>
b5_LP-12_T16 (L-21b)		2458	<b>898</b>	<b>2.47</b>	116	3.53
b5_LP-12_T20 (L-22b)		2475	987	2.51	119	3.74
SIMD (8b/16b/32b)		Accurate (R4BM)	6163	1875	2.5	569
	LP-8 (L-1)	4390	1990	5.5	252	7.6
	LP-12 (L-2)	4810	1840	5.55	255.5	7.9
	LP-12_T16 (L-21)	4310	1930	5.3	245.5	6.9
	LP-12_T20 (L-22)	4470	2020	5.7	260	8.5
	<b>b5_LP-8 (L-1b)</b>	<b>3028</b>	1396	3.16	<b>126.8</b>	4.22
	b5_LP-12 (L-2b)	3349	1286	3.28	135.7	4.86
	<b>b5_LP-12_T16 (L-21b)</b>	<b>3020</b>	1318	<b>3.04</b>	128.1	<b>3.94</b>
	b5_LP-12_T20 (L-22b)	3142	1494	3.22	134.2	4.63
	<b>TCAS-II'24 [35]</b>	SIMD INT4/FP8/16/32	8054	1718	4.62	296
<b>TVLSI'22 [37]</b>	SIMD FP16/32/64	8065	1072	5.56	376	11.6
<b>TCAS-II'22 [4]</b>	Posit-FP8/16/32	5972	1634	3.74	499	7

SIMD engines. These gains arise from applying approximation and bounded-regime simplification across multiple stages of the Posit datapath, rather than only replacing the mantissa multiplier. The resulting FPGA implementation provides a favorable area-power trade-off for precision-reconfigurable Posit NCEs, with the application-level impact of the introduced arithmetic error evaluated in Section IV-D.

### C. ASIC Results

The RTL was synthesized and placed-and-routed using a Cadence RTL-to-GDS flow, with Genus for logic synthesis

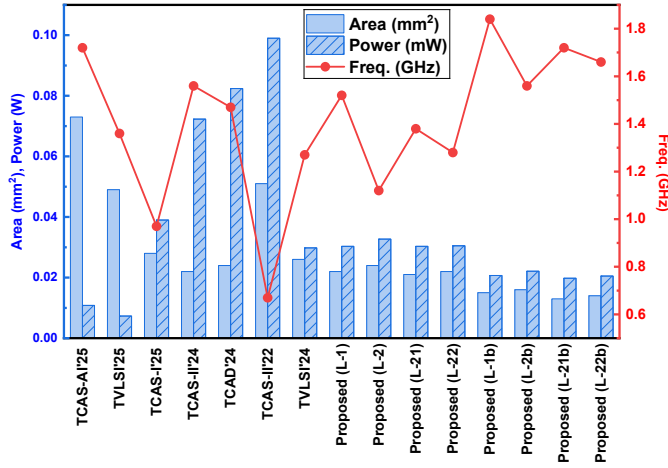


Fig. 6. Comparative 28-nm ASIC resource consumption against state-of-the-art SIMD NCEs [4], [8], [33], [38]–[42].

and Innovus for place-and-route. All ASIC results target a 28-nm CMOS HPC+ process at the TT corner, 25°C, and 0.9 V. Timing, area, and power are reported after place-and-route.

Fig. 6 compares EULER-ADAS against state-of-the-art NCEs. Since Posit-8/16/32 can provide dynamic range comparable to FP-16/32/64 at lower bit width [35], [38], the proposed design supports a wide precision range while occupying less silicon area than the designs in [38], [39]. EULER-ADAS also achieves a higher operating frequency than the exact Posit design in [4] and lower power than the designs in [40], [41]. These gains come from co-optimizing the full Posit NCE datapath: exact mantissa multiplication is replaced with stage-adaptive logarithmic multiplication, bounded-Posit representation simplifies decoding and encoding, and a shared accumulation path is preserved across all precision modes.

Table III compares error metrics and 28-nm ASIC resource consumption for prior approximate multipliers integrated into the same SIMD NCE context. Bold entries highlight the best prior reference points and the proposed values emphasized in the discussion. The proposed bounded variants (L-1b through L-22b) occupy 0.013–0.016 mm<sup>2</sup> and consume 19.8–22.1 mW, reducing area and power by up to 75% and 80%, respectively, relative to the exact baseline. Compared with the most compact prior design in the table, ACMLC at 0.026 mm<sup>2</sup> and 38.9 mW, the bounded EULER-ADAS variants reduce both area and power by approximately half. The non-bounded variants occupy 0.021–0.024 mm<sup>2</sup> and consume 30.3–32.7 mW while operating at up to 1.52 GHz. Although some proposed variants exhibit higher fixed-point MAE than prior approximate multipliers, their Posit-domain MSE remains low, indicating that large-magnitude Posit errors are limited and supporting the use of MSE as the primary arithmetic fidelity metric for DNN inference.

Table IV reports operating frequency, power, area, throughput, energy efficiency, and compute density under fully pipelined steady-state execution. Throughput scales with SIMD lane parallelism, with the highest GOPS obtained in Posit-8 mode and proportionally lower values in Posit-16 and Posit-32 modes. Among prior approximate de-

TABLE III  
ERROR-ASIC RESOURCE (28-NM) TRADE-OFF ANALYSIS: PROPOSED SIMD NCE WITH STATE-OF-THE-ART APPROXIMATIONS [22], [26], [29], [31], [43]–[51].

Design	Fixed-point		Posit		SIMD NCE		
	MAE (%)	MSE (%)	MAE (%)	MSE (%)	Area (mm <sup>2</sup> )	Freq. (GHz)	Power (mW)
Baseline (Exact)	0	0	0.04	0.09	0.052	0.67	99
MITCH_TRUNC	14.43	1.47	8.65	0.52	0.023	1.13	<b>32.7</b>
ROBA	2.92	6.10	2.04	2.10	0.032	0.96	40.8
RAD1024	0.44	1.36	0.31	0.48	0.029	1.04	48.3
ALM_SOA	8.06	4.60	4.31	1.61	0.028	1.12	46.9
HLR_BM	7.20	3.66	3.10	1.12	0.032	0.93	41.5
TOSAM	5.20	2.40	2.66	0.96	0.031	0.99	43.5
HPR-Mul	2.50	1.60	1.48	0.64	0.034	0.89	49.3
ACE	6.10	2.80	3.00	1.08	0.029	1.03	42.0
ACSAM	5.60	2.60	2.76	0.98	0.028	1.04	41.7
ACMLC	7.10	3.30	3.42	1.22	<b>0.026</b>	1.08	38.9
CDM	4.00	2.00	2.18	0.79	0.031	0.96	45.2
FARA	3.90	2.10	2.05	0.80	0.032	0.95	46.0
Proposed (L-1)	15.10	1.21	6.00	0.43	0.022	<b>1.52</b>	30.3
Proposed (L-2)	11.84	<b>0.99</b>	<b>5.04</b>	<b>0.35</b>	0.024	1.12	32.7
Proposed (L-21)	12.70	1.06	5.42	0.39	0.021	1.38	30.3
Proposed (L-22)	12.20	1.01	5.18	0.37	0.022	1.28	30.5
Proposed (L-1b)	15.90	1.27	6.45	0.47	0.015	<b>1.84</b>	20.7
Proposed (L-2b)	12.60	1.04	5.35	0.38	0.016	1.56	22.1
Proposed (L-21b)	13.35	1.10	5.82	0.41	<b>0.013</b>	1.72	<b>19.8</b>
Proposed (L-22b)	12.90	1.08	5.56	0.39	0.014	1.66	20.5

signs, MITCH\_TRUNC provides the highest Posit-8 throughput at 45.2 GOPS, while ACMLC provides the best area among the listed prior designs at 0.026 mm<sup>2</sup>. The proposed non-bounded L-1 configuration reaches 60.8 GOPS at 1.52 GHz and 30.3 mW, corresponding to 2.007 TOPS/W and 0.276 TOPS/mm<sup>2</sup>. The bounded variants improve this trade-off further: L-1b reaches 73.6 GOPS at 1.84 GHz and 20.7 mW, while L-21b achieves the lowest power at 19.8 mW and the highest compute density at 0.529 TOPS/mm<sup>2</sup>. These text-discussed values are bolded in the table, showing that the area and power reductions from bounded encode/decode, logarithmic mantissa multiplication, and shared accumulation translate into improved system-level efficiency across precision modes. An extended ASIC performance comparison of the proposed EULER variants against SIMD approximate NCEs and Posit MPEs is provided in the Supplementary Material.

The stage-wise ASIC resource distribution in Table V presents results under the typical-typical (TT) corner (0.9 V, 25°C), while results for the slow-slow (SS) and fast-fast (FF) corners are provided in the Supplementary Material. EDP is computed as  $EDP = P \cdot D^2$ , where  $D = 1/f$  is the critical-path delay at maximum operating frequency  $f$ , and is reported in units of 10<sup>-5</sup> fJ.s. Bold entries highlight the minimum proposed values in the key stage-wise resource columns. The bounded-Posit input and output processing stages reduce both area and power relative to the corresponding standard-Posit variants, confirming the benefit of simplifying variable-length encode/decode logic. In the mantissa multiplication stage, the

TABLE IV  
ASIC PERFORMANCE METRICS COMPARISON WITH SIMD APPROXIMATE NCEs [22], [26], [29], [31], [43]–[51] AND MPES.

Design	Freq (GHz)	Power (mW)	Area (mm <sup>2</sup> )	Throughput (GOPS)			Energy Efficiency (TOPS/W)			Compute Density (TOPS/mm <sup>2</sup> )		
				TP_P8	TP_P16	TP_P32	EE_P8	EE_P16	EE_P32	CD_P8	CD_P16	CD_P32
<b>Baseline (Exact)</b>	0.67	99	0.052	26.8	12.70	2.82	0.271	0.129	0.0292	0.052	0.0244	0.0052
MITCH_TRUNC	1.13	32.68	0.023	<b>45.2</b>	21.42	4.76	1.383	0.659	0.1490	0.197	0.0931	0.0209
ROBA	0.96	40.84	0.032	38.4	18.20	4.04	0.940	0.448	0.1013	0.120	0.0569	0.0128
RAD1024	1.04	48.25	0.029	41.6	19.72	4.38	0.862	0.411	0.0929	0.143	0.0680	0.0152
ALM_SOA	1.12	46.89	0.028	44.8	21.23	4.72	0.955	0.455	0.1029	0.160	0.0758	0.0168
HLR_BM	0.93	41.46	0.032	37.2	17.63	3.92	0.897	0.427	0.0967	0.116	0.0551	0.0124
TOSAM	0.99	43.5	0.031	39.6	18.76	4.17	0.910	0.431	0.0958	0.128	0.0605	0.0135
ACE	1.03	42.0	0.029	41.2	19.52	4.34	0.981	0.465	0.1034	0.142	0.0673	0.0150
ACSAM	1.04	41.7	0.028	41.6	19.71	4.38	0.998	0.473	0.1049	0.149	0.0704	0.0156
ACMLC	1.08	38.9	<b>0.026</b>	43.2	20.47	4.55	1.110	0.526	0.1170	0.166	0.0787	0.0175
CDM	0.96	45.2	0.031	38.4	18.19	4.05	0.850	0.402	0.0895	0.124	0.0587	0.0131
FARA	0.95	46.0	0.032	38.0	18.00	4.00	0.826	0.391	0.0870	0.119	0.0563	0.0125
TCAS-II'24 [35]	1.47	29.3	0.032	27.9	13.24	2.94	1.760	0.838	0.1896	0.279	0.1324	0.0294
TVLSI'22 [37]	1.43	43.8	0.046	57.2	27.11	6.02	1.306	0.622	0.1407	0.124	0.0589	0.0131
<b>Proposed (L-1)</b>	<b>1.52</b>	<b>30.3</b>	<b>0.022</b>	<b>60.8</b>	<b>28.80</b>	<b>6.40</b>	<b>2.007</b>	<b>0.950</b>	<b>0.211</b>	<b>0.276</b>	<b>0.131</b>	<b>0.029</b>
<b>Proposed (L-2)</b>	1.12	32.7	0.024	44.8	21.22	4.72	1.370	0.649	0.144	0.187	0.088	0.020
<b>Proposed (L-21)</b>	1.38	30.3	0.021	55.2	26.15	5.81	1.822	0.863	0.192	0.263	0.125	0.028
<b>Proposed (L-22)</b>	1.28	30.5	0.022	51.2	24.26	5.39	1.679	0.796	0.177	0.233	0.110	0.025
<b>Proposed (L-1b)</b>	<b>1.84</b>	<b>20.7</b>	0.015	<b>73.6</b>	<b>34.87</b>	<b>7.75</b>	<b>3.556</b>	<b>1.684</b>	<b>0.374</b>	<b>0.491</b>	0.232	0.052
<b>Proposed (L-2b)</b>	1.56	22.1	0.016	62.4	29.56	6.57	2.824	1.338	0.297	0.390	0.185	0.041
<b>Proposed (L-21b)</b>	1.72	<b>19.8</b>	<b>0.013</b>	68.8	32.59	7.24	3.475	1.646	0.366	<b>0.529</b>	<b>0.251</b>	<b>0.056</b>
<b>Proposed (L-22b)</b>	1.66	20.5	0.014	66.4	31.46	6.99	3.239	1.535	0.341	0.474	0.225	0.050

TABLE V  
STAGE-WISE 28-NM ASIC RESOURCE DISTRIBUTION AGAINST STATE-OF-THE-ART SIMD NEURAL COMPUTE ENGINES.

Design	Precision	Stage	S0	S2, S3	S4, S5	S5	Total	Max. Freq. (GHz)	EDP (10 <sup>-5</sup> fJ.s)
			Input Proc.	Mant. Mult. & Exp. Comp.	Accum.	Output Proc.			
TCAD'24 [41]	FP-16/32/64, BF16/TF32	Area ( $\mu\text{m}^2$ )	6575	14735	3058	6320	30688	1.47	3.82
		Power (mW)	24.5	20.5	12.0	25.5	82.5		
TCAS-II'22 [4]	Posit-8/16/32	Area ( $\mu\text{m}^2$ )	8079	22772	13273	5855	49979	0.67	22.2
		Power (mW)	16.2	43.5	26.0	14.0	99.7		
Proposed	L. Posit-8/16/32 (L-1)	Area ( $\mu\text{m}^2$ )	2156	11782	3058	5714	22710	1.52	1.32
		Power (mW)	1.78	11.8	9.2	7.52	30.3		
	L. Posit-8/16/32 (L-2)	Area ( $\mu\text{m}^2$ )	2156	13185	3058	5714	24113	1.12	2.61
		Power (mW)	1.78	14.2	9.2	7.52	32.7		
	L. Posit-8/16/32 (L-21)	Area ( $\mu\text{m}^2$ )	2156	10353	2586	5714	20809	1.38	1.59
		Power (mW)	1.78	12.4	8.6	7.52	30.3		
	L. Posit-8/16/32 (L-22)	Area ( $\mu\text{m}^2$ )	2156	11072	2586	5714	21528	1.28	1.86
		Power (mW)	1.78	13.4	7.8	7.52	30.5		
	L. Posit-8/16/32 (L-1b)	Area ( $\mu\text{m}^2$ )	<b>990</b>	9285	2281	<b>2892</b>	15448	<b>1.84</b>	<b>0.61</b>
		Power (mW)	<b>0.82</b>	9.3	6.8	<b>3.8</b>	20.7		
L. Posit-8/16/32 (L-2b)	Area ( $\mu\text{m}^2$ )	990	9840	2281	2892	16003	1.56	0.91	
	Power (mW)	0.82	10.6	6.8	3.8	22.1			
L. Posit-8/16/32 (L-21b)	Area ( $\mu\text{m}^2$ )	<b>990</b>	<b>7382</b>	<b>1958</b>	<b>2892</b>	<b>13222</b>	1.72	0.67	
	Power (mW)	<b>0.82</b>	<b>8.8</b>	6.4	<b>3.8</b>	<b>19.8</b>			
L. Posit-8/16/32 (L-22b)	Area ( $\mu\text{m}^2$ )	<b>990</b>	8324	<b>1958</b>	<b>2892</b>	14164	1.66	0.74	
	Power (mW)	<b>0.82</b>	10.1	<b>5.8</b>	<b>3.8</b>	20.5			

ILM reduces area by more than 50% and power by about 70% relative to the TCAS-II'22 exact Posit design [4]. The comparison between L-1 and L-2 also illustrates the cost of increasing logarithmic stage count, while the truncated variants show how reducing retained mantissa width can recover part of this overhead.

#### D. Application Accuracy and System-Level Validation

Application-level impact is evaluated using bit-accurate arithmetic models of the proposed EULER-ADAS NCE variants. These models capture the bounded-regime representation, logarithmic mantissa multiplication, truncation, and SIMD

operating modes used in the hardware evaluation. The resulting inference experiments quantify how the arithmetic errors reported in Table I translate into model-level accuracy across representative workloads.

1) *Image Classification Tasks*: Table VI presents application-level accuracy for VGG-16/CIFAR-100, ResNet-50/ImageNet, ViT-B/ImageNet, MobileNetv2/CIFAR-100, and ResNet-18/ImageNet1k, comparing the proposed EULER variants against FP32, BF16, exact Posit, and logarithmic fixed-point baselines across 8-, 16-, and 32-bit precisions.

The reference results show that exact Posit arithmetic preserves inference accuracy across the evaluated models. Exact

TABLE VI  
APPLICATION ACCURACY FOR IMAGE CLASSIFICATION ACROSS  
DIFFERENT PRECISIONS.

Design	Precision	VGG-16 C100	ResNet-50 ImageNet	VIT-B ImageNet	MobileNets2 C100	ResNet-18 IN1k
Standard Ref.	FP32	74.94	75.7	83.6	74.3	65.4
	BF16	74.69	75.45	83.4	74.1	65.1
	Posit-(8,0)	74.56	75.32	83.2	74.0	65.0
	Posit-(16,1)	74.85	75.61	83.5	74.3	65.3
Log-fxp_2	Posit-(32,2)	75.08	75.84	83.7	74.5	65.5
	FxP-8	72.24	73.1	81.0	71.6	62.7
	FxP-16	72.89	73.75	81.7	72.3	63.3
	FxP-32	73.54	74.45	82.4	72.9	64.0
Log-fxp_3	FxP-8	72.34	73.3	81.2	71.7	62.8
	FxP-16	73.14	74.1	82.0	72.5	63.6
	FxP-32	73.74	74.8	82.7	73.1	64.2
	LP-2 (L-1)	72.81	73.58	81.5	72.2	63.3
This Work (Posit-8)	LP-3 (L-2)	<b>73.14</b>	<b>73.9</b>	<b>81.8</b>	<b>72.5</b>	<b>63.6</b>
	LP-3_T4 (L-21)	72.97	73.72	81.6	72.4	63.4
	LP-3_T5 (L-22)	73.05	73.83	81.7	72.5	63.5
	b2_LP-2 (L-1b)	72.68	73.41	81.3	72.1	63.1
	b2_LP-3 (L-2b)	72.95	73.64	81.5	72.4	63.4
	b2_LP-3_T4 (L-21b)	72.79	73.53	81.4	72.2	63.2
	b2_LP-3_T5 (L-22b)	72.87	73.6	81.5	72.3	63.3
	LP-4 (L-1)	73.26	74.03	81.9	72.7	63.7
	LP-6 (L-2)	<b>73.54</b>	<b>74.3</b>	<b>82.2</b>	<b>72.9</b>	<b>64.0</b>
	LP-6_T8 (L-21)	73.36	74.17	82.1	72.8	63.8
This Work (Posit-16)	LP-6_T10 (L-22)	73.44	74.23	82.1	72.8	63.9
	b3_LP-4 (L-1b)	73.12	73.91	81.8	72.5	63.6
	b3_LP-6 (L-2b)	73.31	74.08	82.0	72.7	63.8
	b3_LP-6_T8 (L-21b)	73.2	73.98	81.9	72.6	63.7
	b3_LP-6_T10 (L-22b)	73.27	74.04	81.9	72.7	63.7
	LP-8 (L-1)	73.56	74.33	82.2	73.0	64.0
	LP-12 (L-2)	<b>73.84</b>	<b>74.6</b>	<b>82.5</b>	<b>73.2</b>	<b>64.3</b>
This Work (Posit-32)	LP-12_T16 (L-21)	73.66	74.47	82.4	73.1	64.1
	LP-12_T20 (L-22)	73.73	74.52	82.4	73.1	64.2
	b5_LP-8 (L-1b)	73.42	74.21	82.1	72.8	63.9
	b5_LP-12 (L-2b)	<b>73.61</b>	<b>74.36</b>	<b>82.3</b>	<b>73.0</b>	<b>64.1</b>
	b5_LP-12_T16 (L-21b)	73.52	74.31	82.2	72.9	64.0
	b5_LP-12_T20 (L-22b)	73.57	74.34	82.2	73.0	64.0

Posit-(32,2) matches or slightly exceeds FP32, while Posit-(16,1) and Posit-(8,0) remain close to the FP32 baseline. This confirms that the underlying Posit formats provide sufficient numerical fidelity for the selected classification workloads before introducing logarithmic approximation or bounded-regime constraints.

The proposed EULER-ADAS variants follow the expected precision and approximation trends. Posit-32 configurations incur the smallest accuracy loss, with LP-12 remaining within roughly 1.1 percentage points of FP32 across the five workloads. The corresponding bounded variant adds only a small degradation, reflecting the dynamic-range reduction introduced by the regime bound. Posit-16 configurations remain within approximately 1.5 percentage points of FP32 for the best logarithmic variants, while Posit-8 exhibits a larger accuracy gap because of its limited dynamic range. The best proposed rows for each precision, together with the bounded Posit-32 counterpart discussed above, are highlighted in Table VI. Truncated configurations fall between the lower-stage and higher-stage logarithmic variants, indicating that truncation provides a controllable area-accuracy trade-off. Across the evaluated precisions, the EULER-ADAS variants also outperform logarithmic fixed-point baselines at comparable bit widths, supporting the use of Posit arithmetic as the numerical substrate for approximate DNN inference.

2) *ADAS Application Scenario*: To assess the applicability of the proposed approximate logarithmic multipliers be-

yond image classification, we evaluate additional benchmarks grouped into seven categories covering ADAS and edge-inference workloads. Table VII summarizes the workloads used in the application-level evaluation. The benchmarks are grouped into seven categories that cover ADAS perception, driver monitoring, end-to-end vehicle control, visual-inertial odometry, augmented-reality gaze estimation, and representative edge-inference NLP tasks. The first five categories focus on autonomous-driving perception and control, including object, vehicle, and pedestrian detection; in-cabin monitoring; traffic sign recognition; road and scene perception; and PilotNet-style control from camera inputs. The remaining categories extend the evaluation to localization, gaze estimation, multilingual translation, language modeling, text-to-speech synthesis, and automatic speech recognition.

Table VIII presents the accuracy results across multiplier variants and numerical precisions. The same trend observed in image classification is preserved across the broader workload set. Posit-32 variants remain closest to the FP32 baseline, with the Posit-32 L-2 values highlighted in bold. Posit-16 variants generally retain near-baseline accuracy with modest degradation from logarithmic approximation and bounded-regime encoding. Operand truncation introduces a smaller penalty than reducing the logarithmic stage count, indicating that retained mantissa width can be used as a secondary tuning knob after the stage count is selected. The largest accuracy losses occur in the most aggressive Posit-8 bounded configurations, where limited dynamic range and approximation error compound. Overall, the results indicate that the proposed arithmetic configurations provide useful area and power savings while maintaining acceptable application-level behavior for the evaluated ADAS and edge-inference workloads.

### E. FPGA Prototype

For system-level validation, the EULER-ADAS engine was deployed within the TREA architecture [8] on the Pynq-Z2 for Tiny-YOLOv3 object detection. Table IX compares the measured latency, power, and energy per frame against FPGA and edge-platform implementations reported for the same workload. The best EULER-ADAS prototype, L-21b, achieves 78 ms latency at 0.29 W, corresponding to 22.6 mJ/frame. This is lower in both latency and energy than the compared FPGA designs in [39], [52], despite those designs targeting the larger VC707 platform. The Pynq-Z2 prototype also compares favorably with the listed embedded CPU, GPU, MCU, and vision-board baselines, indicating that the combined B-Posit and approximate logarithmic multiplier approach is suitable for low-power object detection at the edge.

## V. CONCLUSION

This paper presented EULER-ADAS, a SIMD-enabled logarithmic Posit neural compute engine that jointly optimizes operand decoding, mantissa multiplication, quire accumulation, and result encoding for energy-efficient ADAS inference. By combining bounded-regime Posit representation, stage-adaptive logarithmic multiplication, and runtime-configurable

TABLE VII  
BASELINE APPLICATION METRICS ACROSS EVALUATED WORKLOADS AND NUMERICAL PRECISIONS.

Algo ID	Model	Dataset	Task	Metric	FP32	BF16	Posit-8	Posit-16	Posit-32
<b>Object / Vehicle / Pedestrian Detection</b>									
EULER-Algo_1	YOLO-v5	KITTI	Object detection	mAP	81.9	81.5	80.4	81.2	81.7
EULER-Algo_2	Faster R-CNN	ETH	Vehicle detection	Accuracy	92.3	92.0	91.0	91.8	92.1
EULER-Algo_3	Custom SSD	Caltech Pedestrian	Pedestrian detection	mAP	93.4	93.1	92.0	92.9	93.2
				F1-score	0.90	0.89	0.86	0.89	0.90
<b>Driver Monitoring (In-Cabin)</b>									
EULER-Algo_4	HPM	ICT-3DHP	Head estimation	MAE	1.84	1.89	2.05	1.91	1.86
EULER-Algo_5	SVM + MLP	Yale B	Eye gaze / blink	Accuracy	95.1	94.8	93.8	94.7	95.0
EULER-Algo_6	Custom CNN + MLP	In-house	Driver behavior	Accuracy	92.6	92.3	91.0	92.1	92.4
<b>Traffic Sign Recognition</b>									
EULER-Algo_7	Custom CNN	GTSRB, BTSD, STSD	Traffic classification	Accuracy	83.2	82.9	81.6	82.6	83.1
				mAP	84.7	84.3	83.1	84.1	84.5
<b>Road / Scene Perception</b>									
EULER-Algo_8	SAM	Cityscapes	Segmentation	mIoU	96.8	96.5	95.5	96.3	96.6
EULER-Algo_9	LaneNet	Caltech Lane	Lane detection	Accuracy	91.6	91.3	90.2	91.1	91.4
EULER-Algo_10	SDM	KITTI + Cityscapes	Depth + 3D	mAP	93.1	92.8	91.6	92.6	93.0
				Error	5.42	5.55	6.10	5.65	5.48
EULER-Algo_11	MLP	In-house + Cityscapes	Road classification	mIoU	97.1	96.8	95.8	96.6	96.9
<b>End-to-End Driving</b>									
EULER-Algo_12	PilotNet*	Custom dataset	Vehicle Control	MAE	0.091	0.094	0.105	0.095	0.092
<b>VIO &amp; Eye-Gaze</b>									
EULER-Algo_13	UL-VIO	KITTI Odometry	VIO	Trans. Error	2.18	2.24	2.45	2.26	2.21
				Rot. Error	0.52	0.53	0.60	0.54	0.52
EULER-Algo_14	Eye-Gaze AR	XR datasets	Gaze estimation	MSE	0.0294	0.0305	0.0340	0.0308	0.0298
<b>NLP</b>									
EULER-Algo_15	IndicTrans2	Multilingual	Translation	BLEU	41.1	40.6	39.2	40.4	40.9
				NSS	87.36	86.9	85.5	86.8	87.2
EULER-Algo_16	Meta LLaMa 3.2	Pretrained	LLM	BLEU	35.2	34.8	33.5	34.6	35.1
EULER-Algo_17	Coqui XTTS v3	Speech	TTS	MOS	4.2	4.15	3.95	4.12	4.18
EULER-Algo_18	IndicParlerTTS	Indic speech	TTS	NSS	95.36	94.9	93.5	94.8	95.1
				MOS	4.5	4.45	4.25	4.42	4.48
				WER	5.2	5.4	6.1	5.5	5.25
EULER-Algo_19	NLLB-200	Multilingual	Translation	WER	2.9	3.0	3.4	3.1	2.95
EULER-Algo_20	Whisper Large-v3	Speech	ASR	WER	2.9	3.0	3.3	3.1	2.95

SIMD accumulation, the proposed architecture reduces data-path cost while preserving application-level accuracy across representative workloads.

Experimental results show that the proposed bounded-Posit variants achieve up to 55% reduction in LUT utilization, more than 45% lower power consumption, and up to 10 $\times$  lower EDP compared with radix-4 Booth-based Posit multipliers. At the NCE level, the proposed configurations reduce LUT count by up to 41.4%, delay by up to 76.1%, and power by up to 71.9% relative to exact Posit NCEs. In 28-nm ASIC implementation, EULER-ADAS reaches up to 1.84 GHz at 20.7 mW while occupying as little as 0.015 mm<sup>2</sup>.

Across VGG-16, ResNet-50, ViT-B, MobileNet2, and ResNet-18 workloads, the evaluated Posit-16 and Posit-32 configurations remain close to FP32 accuracy, confirming that the introduced arithmetic approximation has limited impact on application-level performance. The bounded-Posit variants also reduce sensitivity to catastrophic regime-field faults while lowering encode/decode complexity. System-level validation using Tiny-YOLOv3 on the Pynq-Z2 platform achieves 78 ms latency, 0.29 W power, and 22.6 mJ/frame for the best configuration, demonstrating the practical deployment potential of EULER-ADAS for low-power edge ADAS workloads.

Future work will focus on post-silicon validation, sparsity-

aware and layer-adaptive runtime precision SIMD scheduling, and evaluation with a complete software stack targeting end-to-end autonomous perception pipelines for ADAS SoCs.

## REFERENCES

- [1] S. Ki, J. Park, and H. Kim, "Dedicated FPGA Implementation of the Gaussian TinyYOLOv3 Accelerator," *IEEE Transactions on Circuits and Systems II: Express Briefs*, vol. 70, no. 10, pp. 3882–3886, 2023.
- [2] J. Sharda, W. Li, Q. Wu, *et al.*, "Temporal Frame Filtering for Autonomous Driving Using 3D-Stacked Global Shutter CIS With IWO Buffer Memory & Near-Pixel Compute," *IEEE Transactions on Circuits and Systems I: Regular Papers*, vol. 70, no. 5, pp. 2074–2084, 2023.
- [3] N. Jouppi, G. Kurian, S. Li, *et al.*, "TPU v4: An Optically Reconfigurable Supercomputer for Machine Learning with Hardware Support for Embeddings," in *Proc. 50th Annu. Int. Symp. Comput. Archit. (ISCA)*, (New York, NY, USA), 2023.
- [4] L. Crespo, P. Tomás, N. Roma, and N. Neves, "Unified Posit/IEEE-754 Vector MAC Unit for Transprecision Computing," *IEEE Trans. Circuits Syst. II, Exp. Briefs*, vol. 69, no. 5, pp. 2478–2482, 2022.
- [5] J. Hu, Z. Zhang, Z. Li, *et al.*, "Single-Step Hardware-Aware NN Quantization with Mixed Precision," *IEEE Trans. Comput.*, 2026.
- [6] Q. Cheng, M. Huang, C. Man, A. Shen, L. Dai, H. Yu, and M. Hashimoto, "Reliability exploration of system-on-chip with multi-bit-width accelerator for multi-precision deep neural networks," *IEEE Transactions on Circuits and Systems I: Regular Papers*, vol. 70, no. 10, pp. 3978–3991, 2023.
- [7] D. Mallasén, R. Murillo, G. Botella, and A. A. Del Barrio, "Navigating posit arithmetic: A comprehensive survey of principles, hardware, and applications," *ACM Comput. Surv.*, vol. 58, Nov. 2025.

TABLE VIII  
PERFORMANCE EVALUATION FOR ADAS ALGORITHMS.

Algo	Metric	Posit-8								Posit-16								Posit-32							
		L-2	L-22	L-21	L-2b	L-22b	L-21b	L-1	L-1b	L-2	L-22	L-21	L-2b	L-22b	L-21b	L-1	L-1b	L-2	L-22	L-21	L-2b	L-22b	L-21b	L-1	L-1b
E1	mAP	80.4	80.3	80.2	80.1	80.0	79.9	79.6	79.4	81.1	81.05	81.0	80.95	80.9	80.85	80.7	80.6	<b>81.6</b>	81.58	81.56	81.54	81.52	81.50	81.45	81.40
E2	Accuracy	91.0	90.9	90.8	90.7	90.6	90.5	90.2	90.0	91.7	91.65	91.6	91.55	91.5	91.45	91.3	91.2	<b>92.0</b>	91.98	91.96	91.94	91.92	91.90	91.85	91.80
E3	mAP	92.0	91.9	91.8	91.7	91.6	91.5	91.2	91.0	92.8	92.75	92.7	92.65	92.6	92.55	92.4	92.3	<b>93.1</b>	93.08	93.06	93.04	93.02	93.00	92.95	92.90
E3	F1-score	0.86	0.85	0.84	0.83	0.82	0.81	0.80	0.78	0.89	0.885	0.88	0.875	0.87	0.865	0.86	0.855	<b>0.90</b>	0.898	0.896	0.894	0.892	0.890	0.888	0.885
E4	MAE	2.05	2.10	2.12	2.15	2.18	2.20	2.25	2.30	1.92	1.94	1.96	1.98	2.00	2.02	2.05	2.08	<b>1.87</b>	1.88	1.89	1.90	1.91	1.92	1.94	1.96
E5	Accuracy	93.8	93.7	93.6	93.5	93.4	93.3	93.0	92.8	94.6	94.55	94.5	94.45	94.4	94.35	94.2	94.1	<b>94.9</b>	94.88	94.86	94.84	94.82	94.80	94.75	94.70
E6	Accuracy	91.0	90.9	90.8	90.7	90.6	90.5	90.2	90.0	92.0	91.95	91.9	91.85	91.8	91.75	91.6	91.5	<b>92.3</b>	92.28	92.26	92.24	92.22	92.20	92.15	92.10
E7	Accuracy	81.6	81.5	81.4	81.3	81.2	81.1	80.8	80.6	82.5	82.45	82.4	82.35	82.3	82.25	82.1	82.0	<b>83.0</b>	82.98	82.96	82.94	82.92	82.90	82.85	82.80
E7	mAP	83.1	83.0	82.9	82.8	82.7	82.6	82.3	82.1	84.0	83.95	83.9	83.85	83.8	83.75	83.6	83.5	<b>84.4</b>	84.38	84.36	84.34	84.32	84.30	84.25	84.20
E8	mIoU	95.5	95.4	95.3	95.2	95.1	95.0	94.7	94.5	96.2	96.15	96.1	96.05	96.0	95.95	95.8	95.7	<b>96.5</b>	96.48	96.46	96.44	96.42	96.40	96.35	96.30
E9	Accuracy	90.2	90.1	90.0	89.9	89.8	89.7	89.4	89.2	91.0	90.95	90.9	90.85	90.8	90.75	90.6	90.5	<b>91.3</b>	91.28	91.26	91.24	91.22	91.20	91.15	91.10
E10	mAP	91.6	91.5	91.4	91.3	91.2	91.1	90.8	90.6	92.5	92.45	92.4	92.35	92.3	92.25	92.1	92.0	<b>92.9</b>	92.88	92.86	92.84	92.82	92.80	92.75	92.70
E10	Error	6.10	6.20	6.25	6.30	6.35	6.40	6.50	6.60	5.70	5.75	5.80	5.85	5.90	5.95	6.00	6.05	<b>5.50</b>	5.52	5.54	5.56	5.58	5.60	5.65	5.70
E11	mIoU	95.8	95.7	95.6	95.5	95.4	95.3	95.0	94.8	96.5	96.45	96.4	96.35	96.3	96.25	96.1	96.0	<b>96.8</b>	96.78	96.76	96.74	96.72	96.70	96.65	96.60
E12	MAE	0.105	0.108	0.110	0.112	0.115	0.118	0.122	0.125	0.096	0.098	0.099	0.101	0.103	0.105	0.108	0.110	<b>0.093</b>	0.094	0.095	0.096	0.097	0.098	0.100	0.102
E13	Trans Err	2.45	2.50	2.52	2.55	2.58	2.60	2.65	2.70	2.28	2.30	2.32	2.34	2.36	2.38	2.40	2.42	<b>2.22</b>	2.23	2.24	2.25	2.26	2.27	2.29	2.30
E13	Rot Err	0.60	0.62	0.63	0.64	0.65	0.66	0.68	0.70	0.55	0.56	0.57	0.58	0.59	0.60	0.62	0.64	<b>0.53</b>	0.54	0.55	0.56	0.57	0.58	0.60	0.62
E14	MSE	0.034	0.035	0.036	0.037	0.038	0.039	0.041	0.043	0.031	0.032	0.033	0.034	0.035	0.036	0.038	0.040	<b>0.030</b>	0.031	0.032	0.033	0.034	0.035	0.037	0.039
E15	BLEU	39.2	39.0	38.8	38.6	38.4	38.2	37.8	37.5	40.3	40.1	39.9	39.7	39.5	39.3	39.0	38.8	<b>40.8</b>	40.7	40.6	40.5	40.4	40.3	40.1	40.0
E15	NSS	85.5	85.3	85.1	84.9	84.7	84.5	84.0	83.5	86.7	86.5	86.3	86.1	85.9	85.7	85.4	85.1	<b>87.1</b>	87.0	86.9	86.8	86.7	86.6	86.4	86.3
E16	BLEU	33.5	33.3	33.1	32.9	32.7	32.5	32.2	32.0	34.5	34.3	34.1	33.9	33.7	33.5	33.2	33.0	<b>35.0</b>	34.9	34.8	34.7	34.6	34.5	34.3	34.2
E17	MOS	3.95	3.90	3.88	3.85	3.82	3.80	3.75	3.70	4.10	4.08	4.06	4.04	4.02	4.00	3.98	3.96	<b>4.15</b>	4.14	4.13	4.12	4.11	4.10	4.08	4.06
E18	NSS	93.5	93.2	93.0	92.8	92.6	92.4	92.0	91.5	94.7	94.5	94.3	94.1	93.9	93.7	93.4	93.1	<b>95.0</b>	94.9	94.8	94.7	94.6	94.5	94.3	94.2
E18	MOS	4.25	4.20	4.18	4.15	4.12	4.10	4.05	4.00	4.40	4.38	4.36	4.34	4.32	4.30	4.28	4.26	<b>4.45</b>	4.44	4.43	4.42	4.41	4.40	4.38	4.36
E18	WER	6.10	6.20	6.25	6.30	6.35	6.40	6.50	6.60	5.60	5.65	5.70	5.75	5.80	5.85	5.90	5.95	<b>5.30</b>	5.32	5.34	5.36	5.38	5.40	5.45	5.50
E19	WER	3.40	3.45	3.48	3.50	3.52	3.55	3.60	3.65	3.10	3.12	3.14	3.16	3.18	3.20	3.22	3.25	<b>3.00</b>	3.02	3.03	3.04	3.05	3.06	3.08	3.10
E20	WER	3.30	3.35	3.38	3.40	3.42	3.45	3.50	3.55	3.10	3.12	3.14	3.16	3.18	3.20	3.22	3.25	<b>3.00</b>	3.02	3.03	3.04	3.05	3.06	3.08	3.10

TABLE IX

LATENCY AND POWER COMPARISON FOR TINY-YOLOV3/PASCAL-VOC (5.6 GOPS REQUIRED PER FRAME) ACROSS FPGA/EDGE PLATFORMS.

Platform / Design	Board / Device	Latency (ms)	Power (W)	Energy (mJ/frame)
<b>This work (L-1)</b>	Pynq-Z2	108	0.44	47.5
<b>This work (L-2)</b>	Pynq-Z2	128	0.53	67.8
<b>This work (L-21)</b>	Pynq-Z2	104	0.42	43.8
<b>This work (L-22)</b>	Pynq-Z2	116	0.48	55.6
<b>This work (L-1b)</b>	Pynq-Z2	82	0.31	25.4
<b>This work (L-2b)</b>	Pynq-Z2	95	0.36	34.2
<b>This work (L-21b)</b>	Pynq-Z2	<b>78</b>	<b>0.29</b>	<b>22.6</b>
<b>This work (L-22b)</b>	Pynq-Z2	86	0.33	28.4
Design-A [39]	VC707	186	2.24	416.6
Design-Edge GPU	Jetson Nano	226	1.34	302.8
Design-MCU + NPU	STM32N6	195	0.90	175.5
Design-CPU	Raspberry Pi	555	2.70	1498.5
Design-B [52]	VC707	772	1.54	1188.9
Design-Arduino-A	Portenta H7	460	2.05	943.0
Design-Arduino-B	Nicla Vision	520	2.88	1497.6

- [8] O. Kokane, M. Lokhande, G. Raut, A. Teman, and S. K. Vishvakarma, "LPRE: Logarithmic Posit-Enabled Reconfigurable Edge-AI Engine," in *Proc. IEEE Int. Symp. Circuits Syst. (ISCAS)*, pp. 1–5, 2025.
- [9] J. Henkel, M. Tahoori, H. Khdr, H. Nassar, V. Meyers, D. Chen, S. Yildirim, Y. Huang, *et al.*, "Invited Paper: Hardware-Software Co-Design for Highly Optimized, Customized, and Reliable AI Systems," in *IEEE/ACM International Conference On Computer Aided Design (ICCAD)*, pp. 1–9, 2025.
- [10] V. Gohil, S. Walia, J. Meki, and M. Awasthi, "Fixed-Posit: A Floating-

Point Representation for Error-Resilient Applications," *IEEE Transactions on Circuits and Systems II: Express Briefs*, vol. 68, no. 10, pp. 3341–3345, 2021.

- [11] A. A. Jonnalagadda, R. Thotli, and J. L. Gustafson, "Closing the gap between float and posit hardware efficiency," *arXiv preprint arXiv:2603.01615*, 2026.
- [12] V. Mishra, M. Traiola, A. Kritikakou, F. F. dos Santos, and U. Chatterjee, "PC-Posits: Enhanced Soft Error Resilience of Posit Arithmetic Through Analytical Modeling," 2026.
- [13] V. Leon, M. A. Hanif, G. Armeniakos, X. Jiao, M. Shafique, K. Pekmetzi, and D. Soudris, "Approximate computing survey, part i: Terminology and software & hardware approximation techniques," *ACM Comput. Surv.*, vol. 57, Mar. 2025.
- [14] T. Zhang, Z. Niu, and J. Han, "A Design Framework for Hardware-Efficient Logarithmic Floating-Point Multipliers," *IEEE Transactions on Emerging Topics in Computing*, vol. 12, no. 4, pp. 991–1001, 2024.
- [15] A. Kumari and R. P. Palathinkal, "Design and Analysis of Energy Efficient Approximate Multipliers for Image Processing and Deep Neural Network," *IEEE Transactions on Circuits and Systems I: Regular Papers*, vol. 72, no. 2, pp. 854–867, 2025.
- [16] D. Danopoulos, G. Zervakis, D. Soudris, and J. Henkel, "TransAxx: Efficient Transformers With Approximate Computing," *IEEE Transactions on Circuits and Systems for Artificial Intelligence*, vol. 2, no. 4, pp. 288–301, 2025.
- [17] S. Shakibhamedan, N. Amirafshar, A. S. Baroughi, H. S. Shahhoseini, and N. TaheriNejad, "ACE-CNN: Approximate Carry Disregard Multipliers for Energy-Efficient CNN-Based Image Classification," *IEEE Transactions on Circuits and Systems I: Regular Papers*, vol. 71, no. 5, pp. 2280–2293, 2024.
- [18] Y. Guo, Q. Zhou, X. Chen, and H. Sun, "Hardware-Efficient Multipliers With FPGA-Based Approximation for Error-Resilient Applications," *IEEE Transactions on Circuits and Systems I: Regular Papers*, vol. 71, no. 12, pp. 5919–5930, 2024.
- [19] Y. Guo, X. Li, X. Luo, H. Sun, H. Waris, and W. Liu, "FPGA-Based Low-Power Signed Approximate Multipliers for Diverse Error-Resilient

- Applications,” *IEEE Transactions on Very Large Scale Integration (VLSI) Systems*, vol. 34, no. 3, pp. 1029–1042, 2026.
- [20] H. Jiang *et al.*, “An efficient approximate radix-8 booth multiplier for edge detection in bioimages by field programmable gate array,” *IEEE Transactions on Circuits and Systems II: Express Briefs*, 2025.
- [21] Q. Cheng, L. Dai, M. Huang, A. Shen, W. Mao, M. Hashimoto, and H. Yu, “A Low-Power Sparse CNN Accelerator With Pre-Encoding Radix-4 Booth Multiplier,” *IEEE Transactions on Circuits and Systems II: Express Briefs*, vol. 70, no. 6, pp. 2246–2250, 2023.
- [22] V. Leon, G. Zervakis, D. Soudris, and K. Pekmestzi, “Approximate Hybrid High Radix Encoding for Energy-Efficient Inexact Multipliers,” *IEEE Transactions on Very Large Scale Integration (VLSI) Systems*, vol. 26, no. 3, pp. 421–430, 2022.
- [23] F. Sabetzadeh, M. H. Moaiyeri, and M. Ahmadinejad, “An Ultra-Efficient Approximate Multiplier With Error Compensation for Error-Resilient Applications,” *IEEE Transactions on Circuits and Systems II: Express Briefs*, vol. 70, no. 2, pp. 776–780, 2023.
- [24] Q. He, Y. Zhao, Z. Zhang, G. Du, X. Nie, *et al.*, “A Cost and Speed Co-Optimized Parallel Stochastic Multiplier for Binary Inputs Supporting Variable Bit-Widths,” *IEEE Transactions on Circuits and Systems II: Express Briefs*, vol. 72, no. 8, pp. 1068–1072, 2025.
- [25] J. N. Mitchell, “Computer Multiplication and Division Using Binary Algorithms,” *IRE Transactions on Electronic Computers*, vol. EC-11, no. 4, pp. 512–517, 1962.
- [26] W. Liu, J. Xu, D. Wang, C. Wang, P. Montuschi, and F. Lombardi, “Design and Evaluation of Approximate Logarithmic Multipliers for Low Power Error-Tolerant Applications,” *IEEE Transactions on Circuits and Systems I: Regular Papers*, vol. 65, no. 9, pp. 2856–2868, 2018.
- [27] W. Zhang, X. Geng, X. Hu, *et al.*, “LUT-ALMs: Trading Off Accuracy and Power for Approximate Logarithmic Multipliers via LUT Optimization,” *IEEE Trans. Comput.*, 2026.
- [28] R. Pilipović, P. Bulić, and U. Lotrič, “A Two-Stage Operand Trimming Approximate Logarithmic Multiplier,” *IEEE Trans. Circuits Syst. I, Reg. Papers*, vol. 68, no. 6, pp. 2535–2545, 2021.
- [29] P. Yin, C. Wang, H. Waris, W. Liu, Y. Han, and F. Lombardi, “Design and Analysis of Energy-Efficient Dynamic Range Approximate Logarithmic Multipliers for Machine Learning,” *IEEE Transactions on Sustainable Computing*, vol. 6, no. 4, pp. 612–625, 2021.
- [30] “An iterative logarithmic multiplier,” *Microprocessors and Microsystems*, vol. 35, no. 1, pp. 23–33, 2011.
- [31] M. S. Kim, A. A. D. Barrio, L. T. Oliveira, R. Hermida, and N. Bagherzadeh, “Efficient Mitchell’s Approximate Log Multipliers for Convolutional Neural Networks,” *IEEE Trans. Comput.*, vol. 68, no. 5, pp. 660–675, 2019.
- [32] Z. Li, Z. Lu, W. Jia, R. Yu, H. Zhang, G. Zhou, Z. Liu, and G. Qu, “Efficient Approximate Floating-Point Multiplier With Runtime Reconfigurable Frequency and Precision,” *IEEE Transactions on Circuits and Systems II: Express Briefs*, vol. 71, no. 7, pp. 3533–3537, 2024.
- [33] S. Kim, C. J. Norris, J. I. Oelund, and R. A. Rutenbar, “Area-Efficient Iterative Logarithmic Approximate Multipliers for IEEE 754 and Posit Numbers,” *IEEE Trans. Very Large Scale Integr. (VLSI) Syst.*, vol. 32, no. 3, pp. 455–467, 2024.
- [34] V. Trivedi, G. Raut, B. Mohammad, S. K. Vishvakarma, and A. Kumar, “C-SIMD: CORDIC-Driven SIMD Processing Element for Resource-Efficient Multi-Precision DL Inference,” *IEEE Access*, 2026.
- [35] B. Li, K. Li, J. Zhou, *et al.*, “A Reconfigurable Processing Element for Multiple-Precision Floating/Fixed-Point HPC,” *IEEE Trans. Circuits Syst. II, Exp. Briefs*, vol. 71, no. 3, pp. 1401–1405, 2024.
- [36] G. Dias, L. Crespo, *et al.*, “Reconfigurable FPU With Precision Auto-Tuning for Next-Generation Transprecision Computing,” *IEEE Trans. Circuits Syst. I, Reg. Papers*, vol. 73, no. 3, pp. 1553–1564, 2026.
- [37] W. Mao, K. Li, Q. Cheng, L. Dai, B. Li, X. Xie, H. Li, L. Lin, and H. Yu, “A Configurable Floating-Point Multiple-Precision Processing Element for HPC and AI Converged Computing,” *IEEE Trans. Very Large Scale Integr. (VLSI) Syst.*, vol. 30, no. 2, pp. 213–226, 2022.
- [38] F. Niknia, Z. Wang, S. Liu, P. Reviriego, Z. Gao, P. Montuschi, and F. Lombardi, “A Configurable Floating-Point Fused Multiply-Add Design With Mixed Precision for AI Accelerators,” *IEEE Trans. Circuits Syst. AI*, vol. 2, no. 3, pp. 248–261, 2025.
- [39] M. Lokhande, G. Raut, and S. K. Vishvakarma, “Flex-PE: Flexible and SIMD Multiprecision Processing Element for AI Workloads,” *IEEE Trans. Very Large Scale Integr. (VLSI) Syst.*, vol. 33, no. 6, pp. 1610–1623, 2025.
- [40] H. Tan, J. Zhang, X. He, *et al.*, “A Low-Cost Floating-Point FMA Unit Supporting Package Operations for HPC-AI Applications,” *IEEE Trans. Circuits Syst. II, Exp. Briefs*, vol. 71, no. 7, pp. 3488–3492, 2024.
- [41] H. Tan, L. Huang, Z. Zheng, H. Guo, *et al.*, “A Low-Cost Floating-Point Dot-Product-Dual-Accumulate Architecture for HPC-Enabled AI,” *IEEE Trans. Comput.-Aided Design Integr. Circuits Syst.*, vol. 43, no. 2, pp. 681–693, 2024.
- [42] M. Sinigaglia, A. Kiamarzi, M. Bertuletti, L. Ghionda, *et al.*, “Maestro: A 302 GFLOPS/W and 19.8 GFLOPS RISC-V Vector-Tensor Architecture for Wearable Ultrasound Edge Computing,” *IEEE Trans. Circuits Syst. I, Reg. Papers*, vol. 72, no. 11, pp. 6665–6678, 2025.
- [43] H. Waris, C. Wang, and W. Liu, “Hybrid Low Radix Encoding-Based Approximate Booth Multipliers,” *IEEE Transactions on Circuits and Systems II: Express Briefs*, vol. 67, no. 12, pp. 3367–3371, 2023.
- [44] R. Zendegani, M. Kamal, M. Bahadori, A. Afzali-Kusha, and M. Pedram, “RoBA Multiplier: A Rounding-Based Approximate Multiplier for High-Speed yet Energy-Efficient Digital Signal Processing,” *IEEE Transactions on Very Large Scale Integration (VLSI) Systems*, vol. 25, no. 2, pp. 393–401, 2021.
- [45] S. Vahdat, M. Kamal, A. Afzali-Kusha, and M. Pedram, “TOSAM: An Energy-Efficient Truncation- and Rounding-Based Scalable Approximate Multiplier,” *IEEE Transactions on Very Large Scale Integration (VLSI) Systems*, vol. 27, no. 5, pp. 1161–1173, 2019.
- [46] A. Sadeghi, R. Rasheedi, I. Partin-Vaisband, and D. Pal, “Energy Efficient Compact Approximate Multiplier for Error-Resilient Applications,” *IEEE Transactions on Circuits and Systems II: Express Briefs*, vol. 71, no. 12, pp. 4989–4993, 2024.
- [47] V. Joshi, A. Agarwal, and P. Mane, “Design and analysis of an accuracy configurable fast approximate recursive multiplier,” *Circuits, Systems, and Signal Processing*, pp. 1–32, 2025.
- [48] N. Amirafshar, A. S. Baroughi, *et al.*, “Carry Disregard Approximate Multipliers,” *IEEE Transactions on Circuits and Systems I: Regular Papers*, vol. 70, no. 12, pp. 4840–4853, 2023.
- [49] S. Shakibhamedan, N. Amirafshar, A. S. Baroughi, *et al.*, “ACE-CNN: Approximate Carry Disregard Multipliers for Energy-Efficient CNN-Based Image Classification,” *IEEE Transactions on Circuits and Systems I: Regular Papers*, vol. 71, no. 5, pp. 2280–2293, 2024.
- [50] V. Trivedi and S. K. Vishvakarma, “ACSAM: Accuracy-configurable Segmentation-based Approximate Multiplier for Error-resilient Edge-AI Applications,” *IEEE Embedded Systems Letters*, pp. 1–1, 2026.
- [51] J. Vafaei and O. Akbari, “HPR-Mul: An Area and Energy-Efficient High-Precision Redundancy Multiplier by Approximate Computing,” *IEEE Transactions on Very Large Scale Integration (VLSI) Systems*, vol. 32, no. 11, pp. 2012–2022, 2024.
- [52] O. Kokane, G. Raut, S. Ullah, M. Lokhande, A. Teman, A. Kumar, and S. K. Vishvakarma, “Retrospective: A CORDIC Based Configurable Activation Function for NN Applications,” in *2025 IEEE Computer Society Annual Symposium on VLSI (ISVLSI)*, vol. 1, pp. 1–6, 2025.



**Mukul Lokhande** (Member, IEEE) received the B.Tech. degree in Electronics and Communication Engineering from SGGSI&T, Nanded, India, in 2020. He submitted his doctoral dissertation at IIT Indore, India, in December 2025, and is currently with Qualcomm Technologies, Inc., Bengaluru, India.

His research interests include hardware-software codesign for efficient edge-AI workloads, multi-precision NPU architectures, approximate arithmetic engines, and digital processing-in-memory architectures.

tures.



**Ratko Pilipović** received the B.Sc. and M.Sc. degrees from the Faculty of Electrical Engineering, University of Banja Luka, Bosnia and Herzegovina, in 2015 and 2017, respectively.

He received the Ph.D. degree from the Faculty of Computer and Information Science, University of Ljubljana, Slovenia, in 2021, where he is currently an Assistant Professor. His research interests include approximate computing, arithmetic circuit design, FPGA design, embedded processing, machine learning, and quantum computing.



**Omkar Kokane** received the B.Tech. degree in Electronics and Communication Engineering from IIIT Pune, India, and the M.Tech. degree in VLSI Design and Nanoelectronics from IIT Indore, India, in 2022 and 2025, respectively.

He is currently pursuing the Ph.D. degree with the PULP Team at the University of Bologna, Italy. His research interests include matrix computation, RISC accelerator extensions, approximate computing, CORDIC-based computation, and reconfigurable design.



**Adam Teman** (Senior Member, IEEE) received the Ph.D. degree in Electrical and Computer Engineering from Ben-Gurion University of the Negev, Israel, in 2014. He is a Full Professor at Bar-Ilan University, a Co-Director of the EnICS Laboratories, and a Co-Founder of RAAAM Memory Technologies, Petach Tikva, Israel.

He has authored more than 115 publications and holds 11 patents. His research interests include embedded memories, energy-efficient circuit design, AI hardware accelerators, and physical design methodologies.

He received the Krill Prize for Outstanding Young Researchers in 2020. Prof. Teman is an Associate Editor of IEEE TCAD.



**Santosh Kumar Vishvakarma** (Senior Member, IEEE) received the Ph.D. degree from the Indian Institute of Technology Roorkee, India, in 2010. From 2009 to 2010, he was with the University Graduate Centre, Norway, as a Postdoctoral Fellow under a European Union project.

He is a Professor in the Department of Electrical Engineering at the Indian Institute of Technology Indore, India, and leads the Nanoscale Devices, VLSI Circuit, and System Design Laboratory. His research interests include processing-in-memory designs and

resource-efficient circuits for edge-AI applications.